

Mid-Infrared Imaging of Alpha Orionis

S. A. Rinehart, T. L. Hayward, J. R. Houck
Cornell University

ABSTRACT

We have imaged the M2Iab supergiant star α Ori at 11.7 μm and 17.9 μm using the Hale 5-m telescope and an array camera with sub-arcsecond angular resolution. Our images reveal the circumstellar dust shell extending out to $\sim 5''$ from the star. By fitting two multi-parameter models to the data, we find values for the dust shell inner radius, the temperature at this radius, the percentage flux produced by the circumstellar material at each of our wavelengths, and the radial dependence of the dust mass density. We present profiles of the mean surface brightness as a function of radius and the power detected from within annular rings as a function of radius.

Subject headings: α Ori – stars: circumstellar shells – dust

1. Introduction

As stars ascend the asymptotic giant branch (AGB), they shed mass, developing a circumstellar shell consisting of atomic gas, molecular gas, and dust. One of the most frequently studied AGB stars is the oxygen-rich M2 Iab star α Ori, which is relatively easily observed due to its high luminosity and proximity, $d \simeq 130$ pc (where $1'' = 130$ AU). Observations of its spatially extended circumstellar shell have been made in many wavelength bands. Mapping at 21 cm has shown that H I emission extends $\sim 1'$ from the star (Bowers & Knapp 1987). Large beam far-IR spectra have detected [C I] 609 μm in the shell (Huggins et al. 1994) as well as [O I] 63 μm and [Si II] 35 μm from what is believed to be the region between the chromosphere and the extended shell (Haas & Glassgold 1993). In the 10 μm band, the shell has been observed using both interferometric (Bester et al. 1996) and drift scan (Bloemhof et al. 1984) techniques, and long-slit 7–14 μm spectra have revealed spatially extended emission from silicate grains (Sloan et al. 1993).

Despite the quantity of previous observations, there are still many unanswered questions about the morphology and the optical properties of the dust. The drift scans taken by Bloemhof et al. (1984) indicate an asymmetry in the dust shell, implying possible smaller scale structure in the circumstellar envelope; however, no fully sampled, sub-arcsecond resolution map of the shell has been published. In addition, the size, temperature distribution, and dust condensation radius of the silicate grains have not been determined.

This paper reports the first successful attempt to spatially resolve the dust cloud surrounding α Ori by direct imaging in the mid-IR. We also present several physical models fit to our observations.

2. Observations and Data Reduction

The observations were made using SpectroCam-10 (Hayward et al. 1993) at the Cassegrain focus of the Hale 5-m telescope.¹ The angular size of the 128x128 Si:As BIB detector’s pixels ($0''.256$) well samples the diffraction limit of the telescope ($0''.5$ FWHM at $10\ \mu\text{m}$, $0''.9$ FWHM at $18\ \mu\text{m}$), making it possible to resolve the dust shell of the star in the mid-IR. Experience has shown that the diffraction limit is frequently achieved with this system. The observations were made on 1994 November 13 and 15. Data were taken using $11.7\ \mu\text{m}$ and $17.9\ \mu\text{m}$ filters with bandwidths of $\sim 1\ \mu\text{m}$ and $\sim 0.5\ \mu\text{m}$, respectively. The $11.7\ \mu\text{m}$ filter was used for observations on both nights, while the $17.9\ \mu\text{m}$ filter was used only on the second. Observations of α Tau were interleaved with the observations of α Ori on both nights, in order to monitor the point spread function over the course of our observations. An active tip-tilt system was employed, minimizing seeing degradation due to telescope movement, and all observations were made with standard beam-switched chopping and nodding techniques.

Individual exposures of α Ori and α Tau were flat-fielded, coadded, and mosaiced to produce images of α Tau and α Ori at each observed wavelength. In the mosaicing process, each input image was rebinned by a factor of 3, replacing each pixel with 9 pixels (3×3). In this magnification, no interpolation was used; each of the subpixels was assigned a flux equal to the one ninth of the original pixel’s flux value. The images were registered to the nearest subpixel ($0''.083$) and coadded. The final image of α Ori at $11.7\ \mu\text{m}$ consists of 11 coadded frames (total on-source integration time of 26.3 s), and the final image of α Ori at $17.9\ \mu\text{m}$ consists of 9 coadded frames (21.7 s on-source integration). The magnitude of α Tau at each wavelength was determined by interpolating between published values listed by Gezari et al. (1993) between 2.2 and $22\ \mu\text{m}$, and flux-magnitude relations were derived from Cohen et al. (1992). These were used to flux calibrate the images of α Ori at both wavelengths.

3. Analysis

The $11.7\ \mu\text{m}$ and $17.9\ \mu\text{m}$ data are presented in Figures 1 and 2. Panels (a) and (b) of each figure show the α Ori and α Tau mosaics. Figures 1c and 2c display the total fluxes within a series of annuli of radius b and width $w = 1/12''$ around the stars, with the α Tau profiles scaled to

¹Observations at the Palomar Observatory were made as part of a continuing collaborative agreement between the California Institute of Technology, the Jet Propulsion Laboratory, and Cornell University.

match the α Ori photospheric emission. The extra emission from the α Ori shell is clearly seen in both plots.

The mid-infrared emission from α Ori arises from two physically distinct components: the stellar photosphere with a diameter of $0''.044$ (Dyck et al. 1992), which is much smaller than our diffraction limit, and the extended circumstellar material. Our images represent the superposition of these two components as convolved with the instrumental point-spread function (PSF). In principle we can generate an image of the shell by subtracting the point source component, but in practice it is difficult to determine what fraction of the total flux is due to the point source. As an example, Figures 1d and 2d show α Ori after subtracting PSF's derived by scaling the α Tau images to contain 33% of the total (star + shell) α Ori flux at $11.7 \mu\text{m}$ and 45% at $17.9 \mu\text{m}$. (These scaling factors were derived from the spike+ modelling in §3.3.) We found that for $b < 1$ arcsec, such subtractions were very sensitive to the scaling factor, the stability of the seeing (which affected the width of the PSF), and the optical aberrations in the telescope (which caused a three-lobed effect that varied slightly between the two stars, especially apparent at $11.7 \mu\text{m}$). Because the photosphere emission is so bright, small errors in its removal have drastic effects on the remaining faint, extended component. However, at $b > 1$ arcsec, where the photospheric contribution is relatively small, the subtraction results were relatively insensitive to the choice of scaling factor.

Both the 11.7 and $17.9 \mu\text{m}$ images reveal that at $b > 1$ arcsec the shell flux is distributed nearly symmetrically about the star. Unfortunately, the $17.9 \mu\text{m}$ images of both stars contained a filter reflection (at 4% of the flux of the star) to the SE of the star. To reduce the effect of this reflection, we did not use the SE quadrant in computing our $17.9 \mu\text{m}$ radial profiles for the modelling described below.

We first attempted to use maximum entropy and maximum likelihood deconvolution techniques in our analysis, but they did not produce stable results for the low surface brightness shell because of the extremely bright nearby point source. Therefore, we developed a series of multi-parameter models for the shell emission and numerically fitted them to the observational data.

3.1. 3-D Models

The numerical models we developed for α Ori assume the basic geometry shown in Figure 3. The star is a 3600 K blackbody point source. The shell is optically thin to the photospheric radiation with dust temperature given by $T(r) = T_o(r_o/r)^{1/2}$, where r is the distance from the star and T_o is the temperature at the reference radius $r_o = 1''$. The mass density of the dust is taken as $\rho = \rho(r)$; the functional form is dependent upon the model geometry. The dust emissivity $\epsilon(\lambda)$ is the astronomical silicate function from Draine & Lee 1984. The total flux along a line of sight at projected radius b equals the sum of the stellar and integrated dust emission:

$$I_{\lambda}(b)_{\alpha Ori} = I_{\lambda}(b)_{phot} + p \frac{2hc^2}{\lambda^5} \left[\int_{x_i}^{x=\infty} \rho(r) \epsilon(\lambda) [\exp\{hc/\lambda kT(r)\} - 1]^{-1} dx \right] \quad (1)$$

$$\text{where } x_i = \begin{cases} 0 & \text{if } r > r_i \\ \sqrt{r_i^2 - b^2} & \text{if } r < r_i \end{cases} \quad (2)$$

and x is the distance along the line of sight (see Figure 3). The integration begins at $x_i = 0$ for $r > r_i$ and $x_i = \sqrt{r_i^2 - b^2}$ for $r \leq r_i$ (i.e. the value of x at the intersection of the line of sight with the inner radius of the shell). The shell starts at an inner radius $r = r_i$, but the integration is terminated at $x = 8''$, as continuing the integration beyond this point results in no additional flux to 1 part in 10^6 in the models considered. In (1), p is the fraction of the total flux due to extended emission and $I_{\lambda}(b)_{phot}$ is the photospheric flux distribution, defined

$$I_{\lambda}(b)_{phot} = \begin{cases} (1 - p)I_{\lambda_{TOT}} & \text{if } b = 0 \\ 0 & \text{if } b > 0 \end{cases} \quad (3)$$

Performing this integration numerically for an assumed form of $\rho(r)$, we generated a profile of the dust shell emission as a function of the mean radius b . The model was then normalized to the shell's total flux ($pI_{\lambda_{TOT}}$) and added to the point source ($I_{\lambda}(b)_{phot}$). To include observational effects, we converted this one-dimensional profile into a two-dimensional image, then convolved the image with the α Tau point spread function. Lastly, we extracted azimuthally averaged one-dimensional profiles $I_{\lambda}(b)_{CM}$ (CM denotes the convolved model) from the model image for comparison with similar profiles extracted from the original mosaics.

The models were fitted to the data using a downhill simplex minimization method (Press et al. 1988). The simplex method attempts to find the best model by minimizing $\chi^2 = \sum_b \frac{1}{\sigma^2} (1 - \frac{I_{\lambda}(b)_{CM}}{I_{\lambda}(b)_{observed}})^2$. Initially, the uncertainty in each point was given by $\sigma = \text{constant}$, but subsequently we tested several other possible definitions of the uncertainty σ by allowing σ to vary as a function of radius ($\sigma = \sigma(b)$). For each of these cases, however, we found that the parameters returned from the fits were similar for each of our different definitions of σ . We therefore conclude that the fitted parameters are robust against both the model details and the boundary conditions.

3.2. Power-Law Models

Initially, the data were fitted using a simple power-law for the dust density ($\rho \propto r^{-n}$), with an inner radius cutoff. Two models were fitted to the 11.7 and 17.9 μm data separately, and a third model linked the two wavelengths by using common values for the temperature, exponent, and inner radius, but separate flux percentages, $p_{11.7}$ and $p_{17.9}$. The best-fit values of parameters r_i , T_i (the temperature at the inner radius of the dust shell), n , and p ($p_{11.7}$ and $p_{17.9}$ for the two-color model) for these models are listed in Table 1.

The observed and modeled 1–D profiles of the star + shell are plotted in Figure 4. The two-color power law model fits the data quite well, with a χ^2 per degree of freedom value of 1.2 assuming a constant 5% error on all data points. The power-law model has a serious weakness, however: it predicts a value of $0''.07$ for the inner radius of the shell, in contradiction to values of $\sim 1''$ indicated by interferometric observations (Danchi et al. 1994).

3.3. The Spike Models

To resolve the incompatibility of our power law models with previous observations, we tested two thin-shell models. The first model, the spike model, assumed a thin shell with thickness of only $0''.1$. This model did not match the observational data nearly as well as the initial power-law model. The χ^2 value was much larger than that found from the thick shell model (by a factor of roughly 100), and the resulting parameter values (see Table 1), such as $r_i = 4''.5$, are not reasonable, as well as incompatible with the model suggested by Danchi et al (1994). Therefore, we rule out the basic spike model.

The second thin-shell model (hereafter termed the spike+ model) was a combination of the spike and extended shell power-law models. We assumed that both the thin and extended shells began at the same inner radius, r_i , and that the temperatures of the two components were equal at this radius. One additional parameter f_p was introduced to specify the ratio of the density of the thin shell to the density of the extended material ($f_p = \rho_{\text{thin}}/\rho_{\text{thick}}$), giving us $\rho(r) = \rho_{\text{thick}}(f_p\delta(r_i) + r^{-n})$. This model, like the power-law model, was fitted to the $11.7\mu\text{m}$ and $17.9\mu\text{m}$ data separately, then was run with the two wavelengths linked by common values for T_o , r_i , n , and f_p . Numerical results from these models are listed in Table 1 and the azimuthally averaged 1–D profiles are included in Figure 4. The spike+ model also produces a good fit to the observed data, with a χ^2 value of 1.0 per degree of freedom for a uniform 5% error on data points. In addition, the model returned inner radii $r_i \approx 1''$, in good agreement with the interferometric observations.

3.4. 2–D Models

One of the major assumptions made in the model calculations was that the circumstellar dust exists in a spherical shell which starts at a well-defined inner radius and extends to a significant distance from the star. In order to test this assumption, we also tried a model with a disk geometry. Using IRAF software, we measured the eccentricities of both α Ori and α Tau to be ≤ 0.05 at $11.7\mu\text{m}$ and ≤ 0.1 at $17.9\mu\text{m}$, so a disk would have to be nearly face-on. We again fit the disk model at each observed wavelength, and then on both wavelengths simultaneously. Both the single- and two-color models were marginally worse than our spherical shell models (Table 2), with a χ^2 value of 1.4 per degree of freedom. This model is included solely for completeness; since

a number of evolved stars display spherically symmetric dust shells, and disk distributions are not observed in these objects, we believe that the disk model is not a realistic representation.

4. Results and Conclusions

We found that the two-color power-law and the two-color spike+ models fit the α Ori images about equally well (Figure 4). However, because of the disagreement between the power-law models and previous interferometric observations, we feel that the spike+ model better represents the α Ori shell. To examine the shape and character of the modeled dust distributions in more detail, we created PSF-subtracted images using the flux ratios determined by the models. Plots of the mean surface brightness of the dust shell component as a function of radius for both models (the two differ in scaling of the subtracted image of α Tau) at both 11.7 and 17.9 μm are shown in Figure 5.

The ratio of the 11.7 μm flux to the 17.9 μm flux, multiplied by the ratio of the emissivities of the silicate dust grains at these two wavelengths (Draine and Lee 1984), indicates the grain color temperature as a function of radius. The temperature results for both the power-law and spike+ models are presented in Figure 6. Also shown are the effective color temperature profiles of the dust distributions of our best-fit models, calculated numerically using the $\rho(r)$ density distributions and the temperature profile for dust grains in thermal equilibrium, $T = T_o(r_o/r)^{1/2}$.

From our two-color spike+ model fits, we find that the dust shell provides $33\% \pm 3\%$ of the total flux at 11.7 μm and $45\% \pm 4\%$ at 17.9 μm . From the value f_p , the ratio of the density of the thin shell at r_i to the density of the extended material at r_i is $\rho_{\text{thin}} \geq (75 \pm 25)\rho_{\text{thick}}$ (we know that $\rho_{\text{thin}}\Delta r \simeq \text{constant}$, where Δr is the thickness of the thin shell, and are therefore limited by the size of our resolution element). Because of the difference in the extent of the two portions of the model dust distribution, the thin shell component provides only $\sim 40\%$ of the dust shell flux (13% of the total flux) at 11.7 μm and only $\sim 30\%$ of the flux (14% of the total flux) at 17.9 μm .

We also find a value for the inner shell radius of $r_i = 1''.0 \pm 0''.1$. This, unlike our simpler power-law model, agrees well with previous interferometric observations (Bester et al. 1991). While this agreement leads us to believe that this model is a better depiction of the actual dust distribution, the dust grain color temperature at r_i is only 460 K, well below the condensation temperature of ~ 1500 K for silicates (Salpeter 1974). One possible explanation for the low temperature is that a stellar wind has pushed the dust inside one arcsecond into the thin shell now observed. The dust presumably condensed at a much smaller radius, then cooled as it was driven away from the star. This would presuppose that the star has not recently been undergoing heavy mass-loss, so that no new dust has condensed near the star. If this scenario is accurate, then we can estimate how long it has been since the last major mass-loss event. The last major variation in the brightness of α Ori occurred during the period 1941-1945. If this brightness variation corresponds to the last major mass-loss event, the mean velocity required to bring the dust from

this event to $1''$ is 12 km s^{-1} . This velocity is in agreement with the 11 km s^{-1} CO linewidths. It should be mentioned that previous work (Danchi et al. 1994) modeled the circumstellar material as a single thin shell (or possible two thin shells), whereas our work indicates that a significant portion of the dust emission comes from a very large extended shell. This is not a surprising difference, given that the interferometric observations were taken with long baselines, making the observations very insensitive to flux coming from large radii.

While we do not favor the power-law model, it is interesting to note that the power-law model color temperature at the inner shell radius ($r_i = 0''.1$) corresponds well to the condensation temperature for silicate grains. By balancing the flux absorbed by an individual grain with the flux emitted by the grain, we find that reasonable grain radii ($a = 0.01 \mu\text{m}$ and $a = 0.1 \mu\text{m}$) produce temperatures ($T_{dust}(r_i) = 1740 \text{ K}$ and $T_{dust}(r_i) = 1890 \text{ K}$ respectively) which agree with both silicate condensation and our power-law model.

The temperature of the dust at one arcsec from the star (the inner shell radius) is found to be $T_o = 460 \pm 20 \text{ K}$. Examining the spike+ model plots on Figure 6, we see that this temperature is in good agreement with the predicted color temperatures from the $\rho(r)$ distribution, especially for projected radii larger than $1''$. We find an average temperature for the spike+ model of $205 \pm 35 \text{ K}$, compared to $T_{\text{mean}} \approx 300$ of Bester et al. (1991).

The last parameter of the dust shell model which was returned from our minimization method was the exponent of the density dependence upon radius for the extended emission, n . The value of this exponent from our best-fit spike+ model is $n = 0.9 \pm 0.1$. However, $n = 2$ for a shell expanding at constant velocity, and $n = 3/2$ for a shell expanding at the escape velocity. Therefore, any plausible, spherically symmetric, steady state density distribution should have $3/2 \leq n \leq 2$. From this discrepancy, we conclude that the circumstellar dust flow must be episodic. This is not surprising, given that the inner radius of the shell also suggests episodic emission.

The authors would like to thank the staff at Palomar Observatory for their assistance and the referee for helpful comments. Figures 1 and 2 can be found in gif format at <http://www.people.cornell.edu/pages/sr22/Aori>. This research was partly supported by NASA Contract 960803.

REFERENCES

- Bernat, A.P., Hall, D.N.B., Hinkle, K.H., & Ridgeway, S.T. 1979. *ApJ*, 233, L135.
- Bester, M., Danchi, W., Degiacomi, C., Townes, C., & Geballe, T. 1991. *ApJ*, 367, L27.
- Bester, M., Danchi, D.H., Townes, C.H., Degiacomi, C.G., Mékarnia, D., & Geballe, T.R. 1996. *ApJ*, 463, 336.
- Bloemhof, E., Danchi, W., & Townes, C. 1985. *ApJ*, 299, L37.

- Bloemhof, E.E. & Danen, R.M. 1995. ApJ, 440, L93.
- Bloemhof, E.E., Townes, C.H., & Vanderwyck, A.H.B. 1984. ApJ, 276, L21.
- Bowers, P.F. & Knapp, G.R. 1987. ApJ, 315, 305.
- Cohen, M., Walker, R. G., Barlow, M.J., Deacon, J.R. 1992. AJ, 104, 1650.
- Danchi, W., Bester, M., Degiacomi, C., Greenhill, L., & Townes, C. 1994. AJ, 107, 1469.
- Draine, B. T. & Lee, H.M. 1984., ApJ, 285, 89.
- Dyck, H., Benson, J., Ridgway, S., & Dixon, D. 1992. AJ, 104, 1982.
- Gezari, D., Schmitz, M., Pitts, P., & Mead, J. 1993. Catalog of Infrared Observations, Third Edition.
- Goldberg, L. 1984. MNRAS, 96, 366.
- Haas, M.R. & Glassgold, A.E. 1993. ApJ, 410, L111.
- Hagen, W., Stencel, R., & Dickenson, D. 1983. ApJ, 274, 286.
- Hayward, T. L., Miles, J. W., Houck, J. R., Gull, G. E., & Schoenwald, J. 1993. Proc. SPIE 1946, 334.
- Howell, R.R., McCarthy, D.W., & Low F.J. 1981. ApJ, 251, L21.
- Huggins, P.J., Bachiller, R., Cox, P., & Forveille, T. 1994. ApJ, 424, L127.
- Knapp, G & Morris, M. 1985. ApJ, 292, 640.
- Mauron, N., Fort, B., Querci, F., Dreux, M., Fanconnier, T., & Lamy, P. 1984. A&A, 130, 341.
- Press, W., Teukolsky, S., Vetterling, W., & Flannery, B. 1988. *Numerical Recipes in C*, Cambridge University Press, Cambridge.
- Rodgers, B. & Glassgold, A.E. 1991. ApJ, 382, 606.
- Salpeter, E.E. 1974. ApJ, 193, 585.
- Salpeter, E.E., 1977. ARA&A, 15, 267.
- Skinner, C.J. & Whitmore, B. 1987. MNRAS, 224, 335.
- Sloan, G., Grasdalen, G., & LeVan, P. 1993. ApJ, 404, 328.

Fig. 1.— Images at $11.7\mu\text{m}$ of α Ori (a), α Tau (b), and the subtracted image (d) produced with the PSF scaled to 39% of the total flux in the α Ori image. Also presented is a plot of the total flux observed within annuli of inner radius b (c). Each of the images are $13''.3$ on a side; the small bar in the upper right of each image is $1''$ long.

Fig. 2.— Images at $17.9\mu\text{m}$ of α Ori (a), α Tau (b), and the subtracted image (d) produced with the PSF scaled to 49% of the total flux in the α Ori image. Also presented is a plot of the total flux observed within annuli of inner radius b (c). Each of the images are $13''.3$ on a side; the small bar in the upper right of each image is $1''$ long.

Fig. 3.— A diagram of the physical geometry used for our models.

Fig. 4.— Plots of the power emitted by annular rings of α Ori (including the star and the shell), with the best-fit model overlaid (a) for the power-law model at $11.7\mu\text{m}$, (b) for the power-law model at $17.9\mu\text{m}$, (c) for the spike+ model at $11.7\mu\text{m}$ and (d) for the spike+ model at $17.9\mu\text{m}$. Units used in these plots are arbitrary.

Fig. 5.— Plots of the mean flux from the dust shell, produced by subtracting a scaled PSF from the raw image of α Ori, as a function of distance from the star (a) for $11.7\mu\text{m}$ and (b) for $17.9\mu\text{m}$. Also provided is a plot of 25% of the flux of α Tau. Examination of these plots shows that at small radii ($b < 1''$), the implied shell brightness is highly model-dependent, while at large radii ($b > 1''$) the shell brightness is very similar for both models.

Fig. 6.— The color temperature of the dust shell, using a two-point blackbody fit from the PSF-subtracted images. Also plotted are the predicted effective color temperature curves for each model.

Parameter	Model	Spike+	Power-law ^a	Disk ^a	Spike ^a
T_i^b	11.7	445±40 K	930±80 K	750 K	...
	17.9	510 (+70/-50) K	1800 (+1300/-700) K	790 K	...
	Two-Color	460±20 K	1700±700 K	580 K	490 K
r_i^c	11.7	1''1 ± 0''1	0''66 ± 0''1	0''58	...
	17.9	0''9 ± 0''1	0''15(+0''2/ - 0''1)	0''42	...
	Two-Color	1''0 ± 0''1	0''07(+0''3/ - 0''06)	0''49	4''9
n^d	11.7	0.93 (+0.09/-0.06)	2.0 (+0.2/-0.1)	0.8	...
	17.9	0.93±0.13	1.4±0.1	0.22	...
	Two-Color	0.9±0.1	1.0±0.1	0.01	2.1
$p_{11.7}^e$	11.7	0.33 (+0.03/-0.02)	0.35 (+0.03/-0.02)	0.33	...
	Two-Color	0.33±0.03	0.39 (+0.03/-0.05)	0.30	0.05
$p_{17.9}^f$	17.9	0.41±0.04	0.47 (+0.03/-0.04)	0.40	...
	Two-Color	0.45±0.04	0.49±0.05	0.41	0.16
f_p^g	11.7	0.986±0.003
	17.9	0.976 (+0.01/-0.06)
	Two-Color	0.986±0.04
χ^2					
	Two-Color	1.0	1.2	1.4	...

^aThese models are included solely for completeness.

^bThe temperature of the dust at the inner edge of the shell.

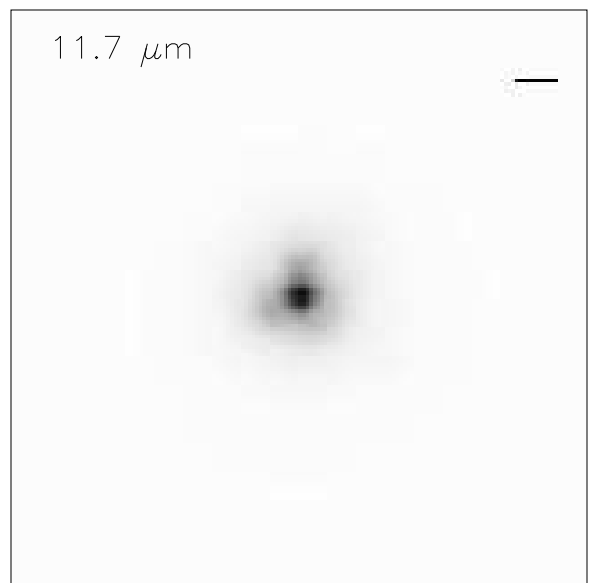
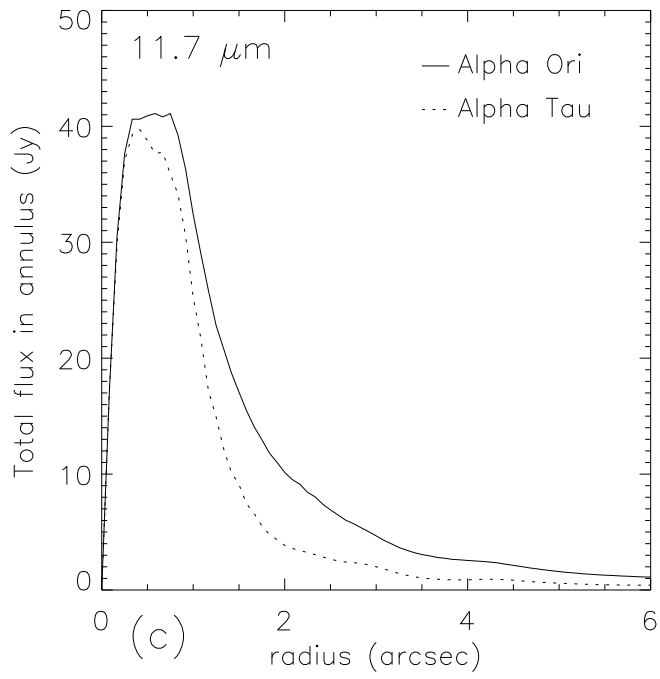
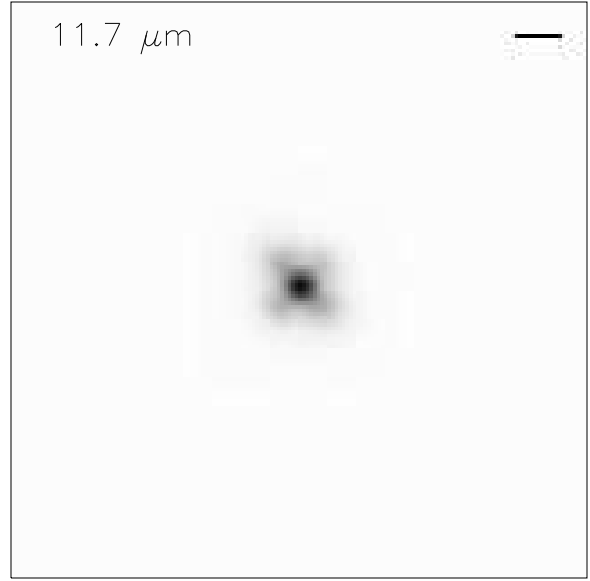
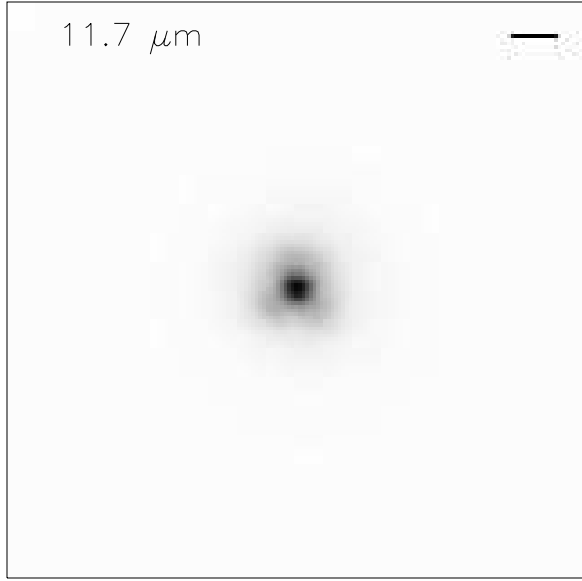
^cThe inner radius of the shell.

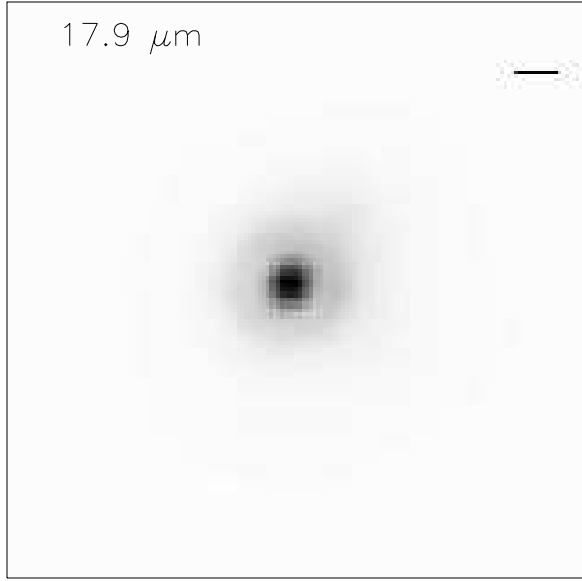
^dThe density power-law exponent.

^eThe fraction of the total α Ori flux from the dust shell at 11.7 μ m.

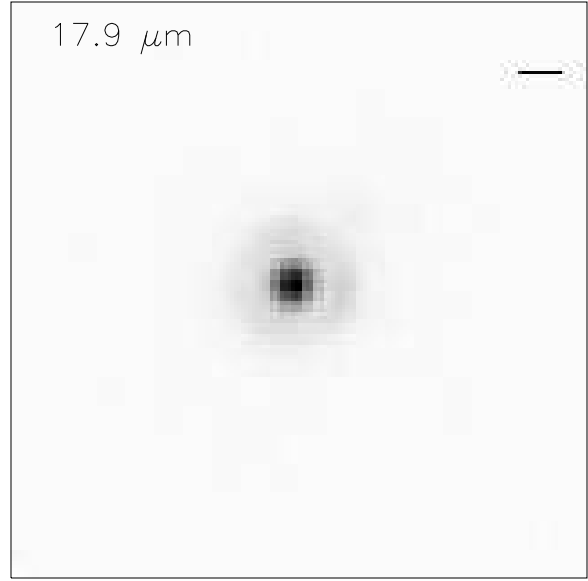
^fThe fraction of the total α Ori flux from the dust shell at 17.9 μ m.

^gThe ratio of the density of the thin shell to the density of the extended shell.

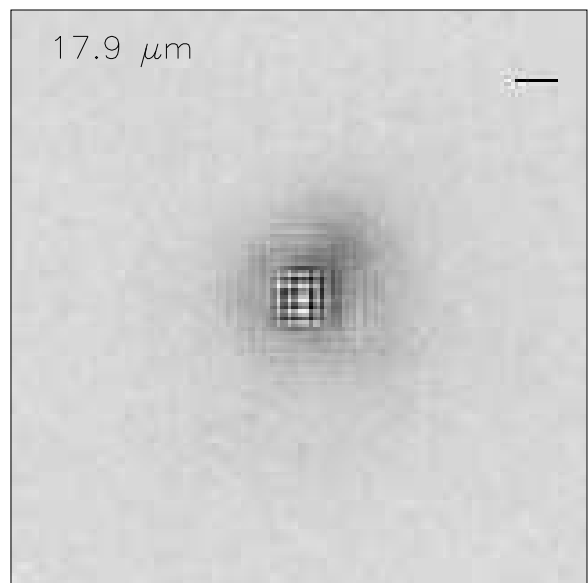
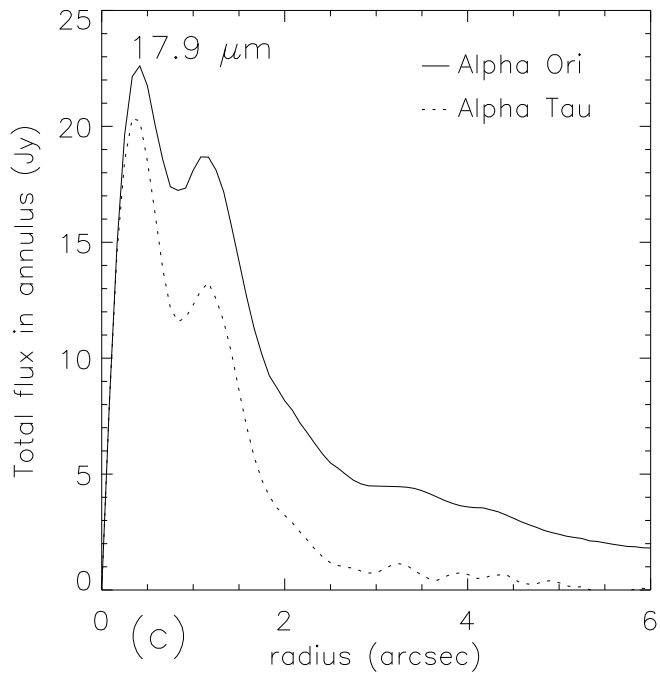




(a)



(b)



(d)

